ACS APPLIED MATERIALS & INTERFACES

Interface Passivation with Codeposition Strategy toward High-Efficiency and Stable Perovskite Solar Cells

Dezhao Zhang, Li He, Haotian Zhang, Hongzhen Su, Yusong Zhou, Wan Li, Shuxin Cui, Hong Liu, and Wenzhong Shen*

Cite This: *ACS Appl. Mater. Interfaces* 2025, 17, 32239−32247

Read Online

ACCESS | Metrics & More | Article Recommendations | Supporting Information

ABSTRACT: The interfaces of each layer in perovskite solar cells (PSCs) are critical factors for efficient and stable perovskite solar cells (PSCs). Especially, poor contact characteristics between perovskite and the electron transport layer in n−i−p-type PSCs significantly affect the carrier dynamics at the buried interface, hindering further improvement in the performance of devices. Herein, we propose a novel codeposition strategy based on (4-bromophenyl) phosphonic acid, which effectively passivates interface and improves the morphology of perovskites, achieving a power conversion efficiency of 24.9%. A part of the molecules spontaneously bond to tin dioxide and act as bridging molecules to connect the tin dioxide layer and perovskite layer during the absorber layer spin-coating process. The phosphonic acid groups and bromine atoms effectively fill oxygen vacancies in tin dioxide and halogen vacancies in the perovskite film. The deprotonated molecules passivate uncoordinated lead defects as passivating agents. The high-efficiency PSCs retained 81% of initial efficiency under ISOS-L-1 MPP tracking for 300h. This approach provides new insights into the interface passivation strategy to realize low-cost and efficient PSCs.

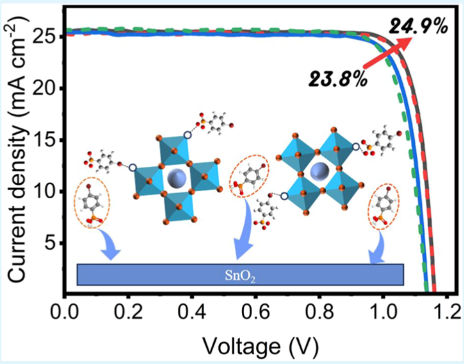

KEYWORDS: *organic additives, codeposition, defect passivation, buried interface, perovskite solar cells*

1. INTRODUCTION

The power conversion efficiency (PCE) of perovskite solar cells (PSCs) has been significantly improved in the past decade, and the certified efficiency has exceeded 26%.[1−5] The PSCs are one of the candidates for next-generation photovoltaics by virtue of their high performance and low-cost manufacturing process. However, the stability and efficiency of PSCs have become bottlenecks for large-scale application.[6−9] The most efficient PSCs manufacturing processes currently rely on layer-by-layer stacking structures, which results in the formation of defects at the interface between the perovskite (PVSK) and carrier transport layers. These defects inhibit the transport of charge carriers and decrease the stability of the devices. The multilayer stacking structure increases the complexity of the fabrication process while reducing the reproducibility of devices.[10−12] Therefore, researchers have developed a codeposition strategy to simplify the stacking procedure and achieve high-efficiency PSCs.

Zheng et al. proposed the codeposition method which was applied to inverted PSCs by incorporating self-assembled molecules (SAMs) into the perovskite precursors, which effectively solves the issue of low wettability.[13] Tang and co-workers successfully achieved the codeposition of organic electron transport materials and perovskite in n−i−p PSCs.[14] The codeposition strategy could construct an efficient and stable interface between organic carrier transport materials and perovskite. However, the codeposition strategy cannot be applied to the PSCs with an inorganic electron transport layer (ETL) in n−i−p PSCs due to the insolubility of ETL (SnO_2, TiO_2) in polar solvents (*N*,*N*-dimethylformamide (DMF), dimethyl sulfoxide (DMSO)). The mainstream approach is to introduce organic additives as a modification layer to passivate the ETL/PVSK interface,[15−17] while the modification layer might be damaged by polar solvents (DMF, DMSO) and possess the issue of low wettability.[18] The codeposition of organic additives and perovskite is a potential approach to overcome these challenges and construct an efficient and stable ETL/PVSK interface.

In this work, we introduced (4-bromophenyl) phosphonic acid (4-PBA) as a perovskite precursor additive to achieve codeposition for passivating the defects of perovskite and tin dioxide (SnO_2). High efficiency and stable PSCs have been achieved by reducing nonradiative recombination losses and enhancing the interface quality. We obtained high-efficiency PSCs with a maximum PCE of 24.9% and excellent long-term

Received: February 2, 2025
Revised: April 23, 2025
Accepted: May 12, 2025
Published: May 20, 2025

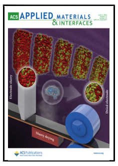

https://doi.org/10.1021/acsami.5c02282

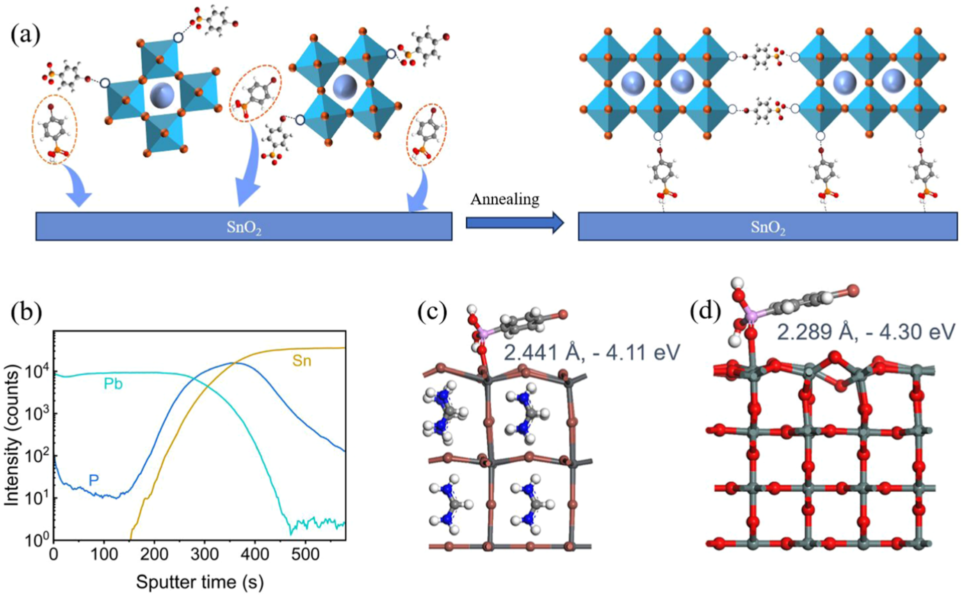

Figure 1. (a) Schematic diagram of the interaction mechanism of 4-PBA during the spin-coating process. (b) spatial distribution of 4-PBA molecules in perovskite as analyzed by time-of-flight secondary ion mass spectrometry (TOF-SIMS) testing; (c) adsorption energy between the 4-PBA molecule and perovskite calculated by density functional theory (DFT); and (d) adsorption energy between the 4-PBA molecule and SnO$_2$ calculated by DFT.

stability, retaining 81% of the initial efficiency under ISOS-L-1 MPP tracking for 300h.

2. RESULTS AND DISCUSSION

2.1. Codeposition of 4-PBA and Perovskite. 4-PBA is a molecule with phosphonic acid groups and bromine atoms, which has been demonstrated to effectively passivate defects in perovskite and SnO$_2$ (Figure S1, Supporting Information).[19,20] The phosphonic acid group can form strong bonding interactions with metal oxides (such as NiO$_x$, SnO$_2$, TiO$_2$, etc.). This characteristic is utilized in the SAMs (Me-2 Pacz, Me-4 Pacz) materials in inverted PSCs.[13,21,22] Moreover, in n−i−p PSCs, molecules with phosphonic acid groups are also commonly used as additives and show self-assembly characteristics.[14,23] Therefore, 4-PBA was added to the perovskite precursor in which the relatively large molecular structure will cause 4-PBA to be squeezed out to the grain boundaries during the crystallization process.[24] It is expected that a part of the molecules will migrate to the SnO$_2$ surface for anchoring, while the rest will exist in the perovskite grain boundaries to passivate defects (Figure 1a).

The spatial distribution of 4-PBA molecules in perovskites was determined by time-of-flight secondary ion mass spectrometry (TOF-SIMS) (Figure 1b). The three-dimensional spatial distribution mapping (Figure S2, Supporting Information) of elements visually illustrates that 4-PBA molecules aggregate at the tin dioxide/perovskite interface, forming a modification layer. Through DFT calculations, the reasons for the aggregation of 4-PBA at the interface have been elucidated. The adsorption energy between 4-PBA and perovskite is −4.11 eV, while the adsorption energy between 4-PBA and SnO$_2$ is −4.30 eV. The difference in adsorption energy indicates that 4-PBA is more inclined to adsorb on the surface of SnO$_2$. Therefore, the rationality of the adsorption mechanism of 4-PBA was proven by experimental and simulation results.

Then, the interaction of 4-PBA with the perovskite precursor was investigated through dynamic light scattering (DLS) measurements. The diameter of colloidal particles in the perovskite precursor increased from 1.3 to 6 nm, and the particle size distribution became more concentrated (Figure S3, Supporting Information), which is conducive to reducing perovskite defects and enhancing uniformity.[25] Fourier transform infrared (FTIR) spectroscopy spectra further elucidated the interaction. The 4-PBA molecules primarily interacted with Pb^{2+}, where the P═O and P−O bonds in the phosphate group engaged with lead ions, resulting in a shift of the P═O and P−O peak positions from 1126 and 1067 cm^{-1} to 1136 and 1072 cm^{-1}, respectively (Figure 2a). However, no significant peak shifts were observed in the FTIR spectra of 4-PBA and formamidinium iodide (FAI), indicating that there is no interaction between 4-PBA and FAI (Figure S4, Supporting Information). Based on the analysis of the X-ray photoelectron spectra (XPS) of perovskite films, the binding energies of Pb 4f shift from 143.2 and 138.4 eV to 142.8 and 138.1 eV, respectively, which is attributed to the increase in electron cloud density around the lead ions induced by the phosphate groups, resulting in a reduction of the binding energy (Figure 2b).[26] Notably, the signal of Pb^0 disappeared in the 4-PBA-doped perovskite films, indicating the enhancement in the stability of the perovskite and suppression of the formation of Pb^0 defects. The shift observed in the XPS spectra of iodine can be attributed to the interaction of halogen bonds between iodine and bromine atoms in 4-PBA (Figure 2c). The interactions can mitigate the formation of harmful I$_2$ in the perovskite and maintain the perovskite structure.[27] Therefore, the interaction between 4-PBA and perovskite is primarily ascribed to the interactions between the phosphonic acid groups and the lead ions as well as between the bromine and iodine atoms.

In order to verify the anchoring effect of 4-PBA molecules on SnO$_2$, the perovskite film was peeled off by ultraviolet adhesive, and the detached SnO$_2$ surface was cleaned with

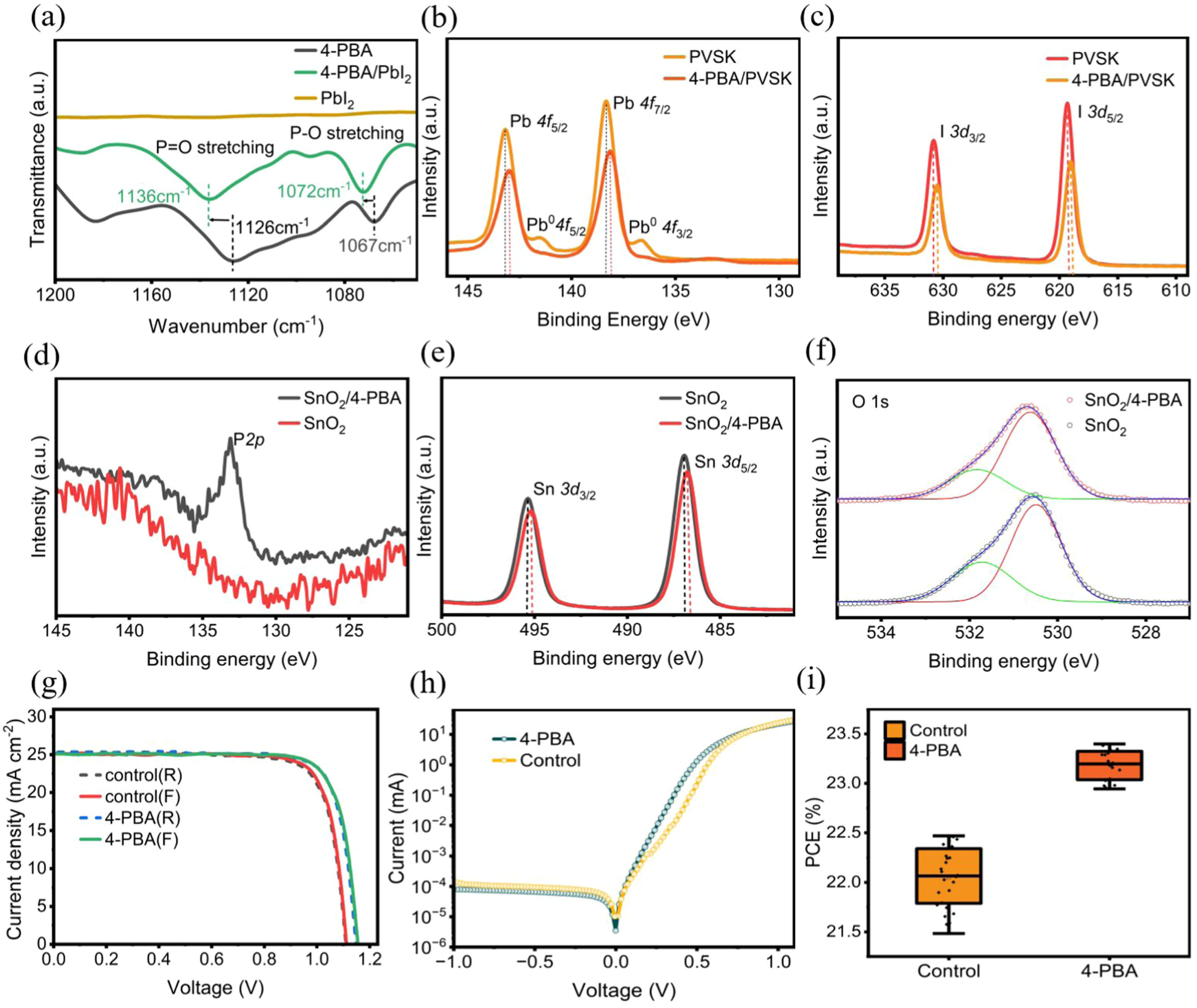

Figure 2. (a) FTIR spetra of undoped PbI_2 and 4-PBA-doped PbI_2; (b, c) XPS spectra of 4-PBA and control PVSK film; (d−f) XPS spectra of detached SnO_2 surface; (g) $J-V$ curve of the device fabricated by redepositing perovskite on detached SnO_2; (h) dark current curve of PSCs; (i) statistics on the efficiencies of PSCs fabricated based on detached SnO_2.

DMF to ensure that no perovskite residues remained on the SnO_2. The unanchored 4-PBA molecules are removed through this method, leaving only the anchored 4-PBA molecules on SnO_2. The presence of lead elements on the surface of SnO_2 was investigated through XPS (Figure S5, Supporting Information). The nearly negligible Pb 4f signal provides evidence that the perovskite was completely removed. The obvious P 2p signal from 4-PBA indicates that a number of 4-PBA molecules are anchored to the surface of SnO_2 (Figure 2d). XPS characterization of Sn 3d and O 1s in SnO_2 films reveals that the coordination of phosphonic acid groups at the surface of SnO_2 with Sn^{4+} results in the shift of the Sn 3d signals from 495.4 and 486.9 eV to 495.1 and 486.6 eV, respectively (Figure 2e). The interaction also induces changes in the energy level structure of the SnO_2 films. The ultraviolet photoelectron spectroscopy (UPS) test results indicate that the work function of the modified SnO_2 decreases, and the Fermi level shifts upward, which is more conducive to the extraction and transport of electrons (Figure S6, Supporting Information). The SnO_2 films can adsorb oxygen from the ambient air due to the presence of oxygen vacancy defects, resulting in the simultaneous presence of signals from lattice oxygen and adsorbed oxygen on the film surface.[23] By fitting the peak of the XPS data of the XPS, the relative content of adsorbed oxygen (O_V, 531.8 eV) and lattice oxygen (O_L, 530.5 eV) can be quantified. The ratio of the corresponding O_V:O_L decreased from 27:73 to 33:67 (Figure 2f).[28] The 4-PBA molecules are anchored on SnO_2 and reduce oxygen vacancy defects, which contribute to the suppression of surface recombination and enhance electron transport.

Therefore, we deposited the perovskite film containing 4-PBA on the substrate and then washed the perovskite films with DMF to obtain the 4-PBA anchored SnO_2 substrate. Subsequently, the perovskite precursor without 4-PBA was spin-coated on the 4-PBA/SnO_2 substrate. After annealing the perovskite films, the deposition of the hole transport layer and metal electrodes was carried out. The $J-V$ testing of PSCs with the fluorine-doped tin oxide (FTO)/SnO_2/4-PBA/PVSK/Spiro-OMeTAD/Ag structure was conducted to verify the passivation effect of 4-PBA on SnO_2. As illustrated in Figure 2g and Table 1, the champion efficiency of the 4-PBA/SnO_2 device is 23.41%, while the SnO_2 device is 22.49%. The enhancement in efficiency primarily is attributed to the increase in open-circuit voltage (V_{OC}), which enhances from 1.112 to 1.155 V. Figure 2h presents the $J-V$ curve of the device in the dark state, where the dark current of the control device is 1.02×10^{-5} mA and that of the target devices is 3.23×10^{-6} mA. The reduction in dark current indicates the passivation effect of 4-PBA on SnO_2. Furthermore, the statistical analysis of 30 devices indicates that the enhancement of PCE primarily arises from an increase in V_{OC} and the hysteresis factor of the 4-PBA-modified devices is smaller (Figures 2i and S7).

Table 1. Efficiency of Champion PSCs Fabricated on SnO_2 and SnO_2/4-PBA Substrates

	V_{OC} (V)	FF (%)	J_{SC} (mA cm^{-2})	PCE (%)
control (F)	1.112	80.31	25.18	22.49
control (F)	1.111	79.16	25.19	22.15
4-PBA (F)	1.155	80.82	25.08	23.41
4-PBA (R)	1.148	80.34	25.35	23.38

2.2. Morphology and Physical Properties of the Perovskite Films. Subsequently, the morphology of the perovskite thin film was characterized by scanning electron microscopy (SEM). The grains of the 4-PBA film appear smoother and more uniform, while the pristine film has a large amount of wrinkles. To observe the bottom surface morphology, the perovskite film was detached by using ultraviolet adhesive. It is evident that the bottom surface of the 4-PBA film shows larger and more compact grains, while that of the pristine film bottom surface contains numerous pinholes, which may lead to increased nonradiative recombination loss (Figure 3a).

The carrier dynamics of the perovskite film was characterized. The test results show that 4-PBA molecules can effectively inhibit the nonradiative recombination of the film and enhance the carrier transport. As shown in Figure 3b, photoluminescence (PL) mapping was carried out on the top and bottom surfaces of the 4-PBA film and the pristine film,

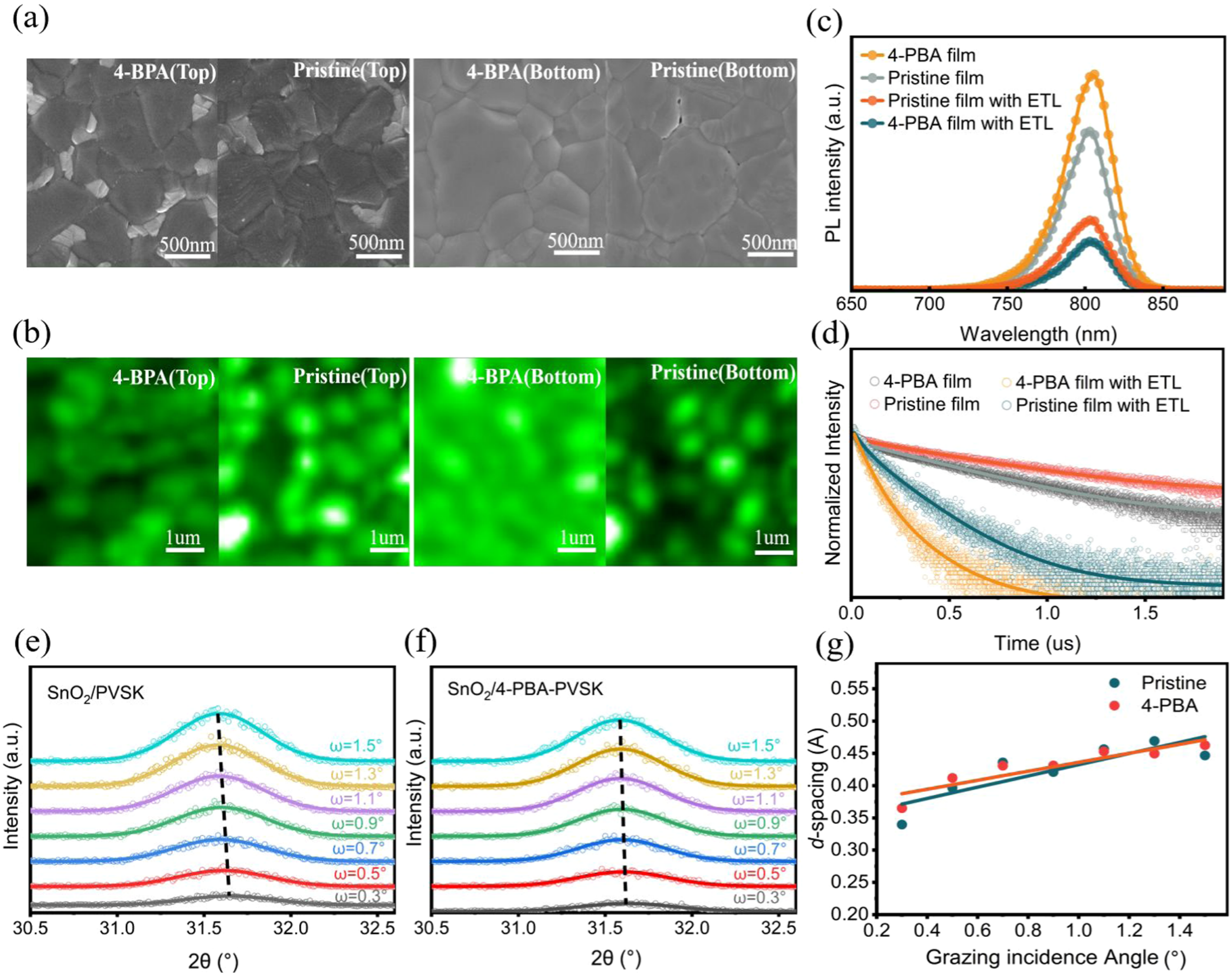

Figure 3. (a) SEM images of top and bottom surface of 4-PBA and pristine film; (b) photoluminescence (PL) mapping of top surface (SnO_2/PVSK and SnO_2/PVSK-4-PBA) and bottom surface (glass/PVSK and glass/PVSK-4-PBA); (c, d) PL and time-resolved photoluminescence (TRPL) spectra of 4-PBA film and pristine film deposited on conductive and insulating substrates; (e, f) grazing incidence X-ray diffraction (GIXRD) spectra of control and target PVSK film; (g) fitting curve of $d-\omega$ plots.

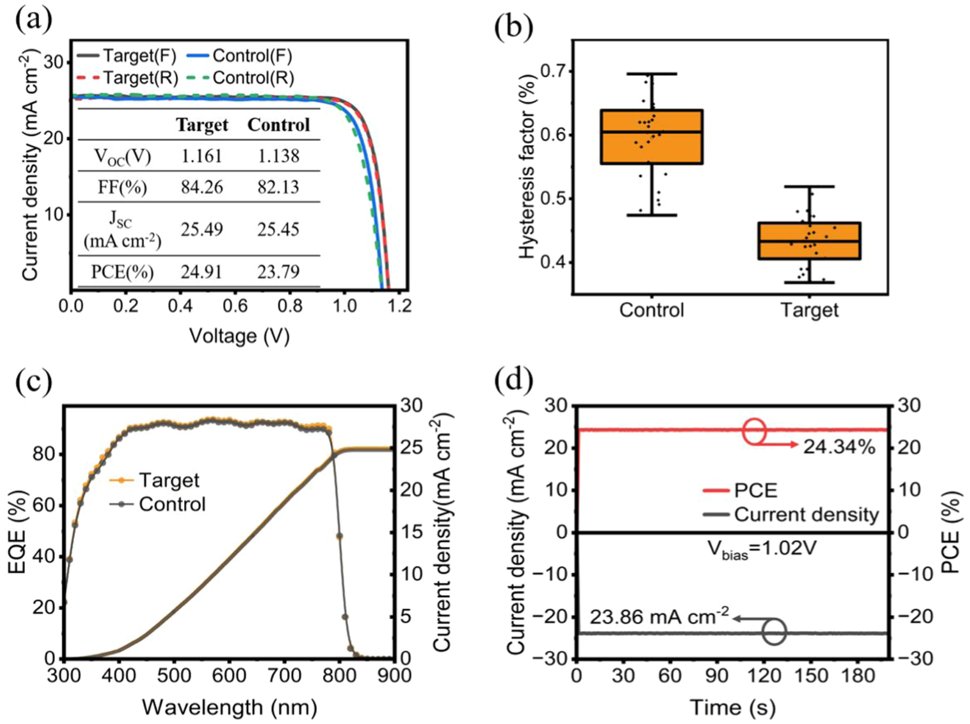

	Target	Control
V_{OC}(V)	1.161	1.138
FF(%)	84.26	82.13
J_{SC} (mA cm^{-2})	25.49	25.45
PCE(%)	24.91	23.79

Figure 4. (a) *J*−*V* curve of the champion efficiency for the control and target devices; (b) statistics of hysteresis factors; (c) external quantum efficiency (EQE) curves of the control and target devices; (d) steady-state output power curve of the champion target device.

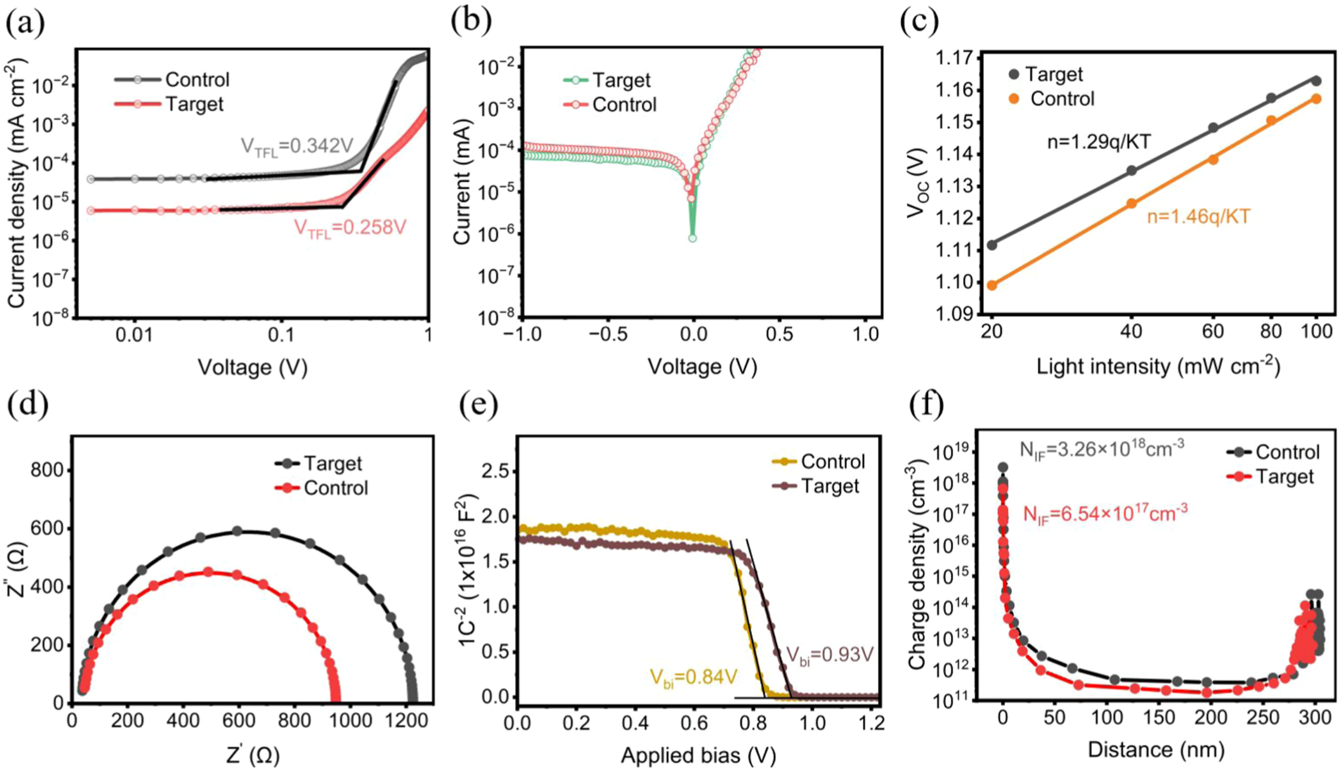

Figure 5. (a) Space-charge-limited current (SCLC) curves of electron-only devices for 4-PBA film and pristine film; (b) dark current curves of the control and target devices; (c) open-circuit voltage versus light intensity dependence curve of the control and target devices; (d−f) electrochemical impedance spectroscopy (EIS) curves, Mott−Schottky curves, and charge density profile curves of the control and target devices.

respectively. The PL intensity of the 4-PBA film deposited on the conductive substrate is significantly lower than that of the pristine film, indicating that the carrier transport has been improved. Then, the perovskite film was peeled off with ultraviolet adhesive, and the exposed bottom surface was measured via PL mapping test. The PL intensity of the 4-PBA film is significantly higher than that of the pristine film, which proves that the nonradiative recombination has been sup-

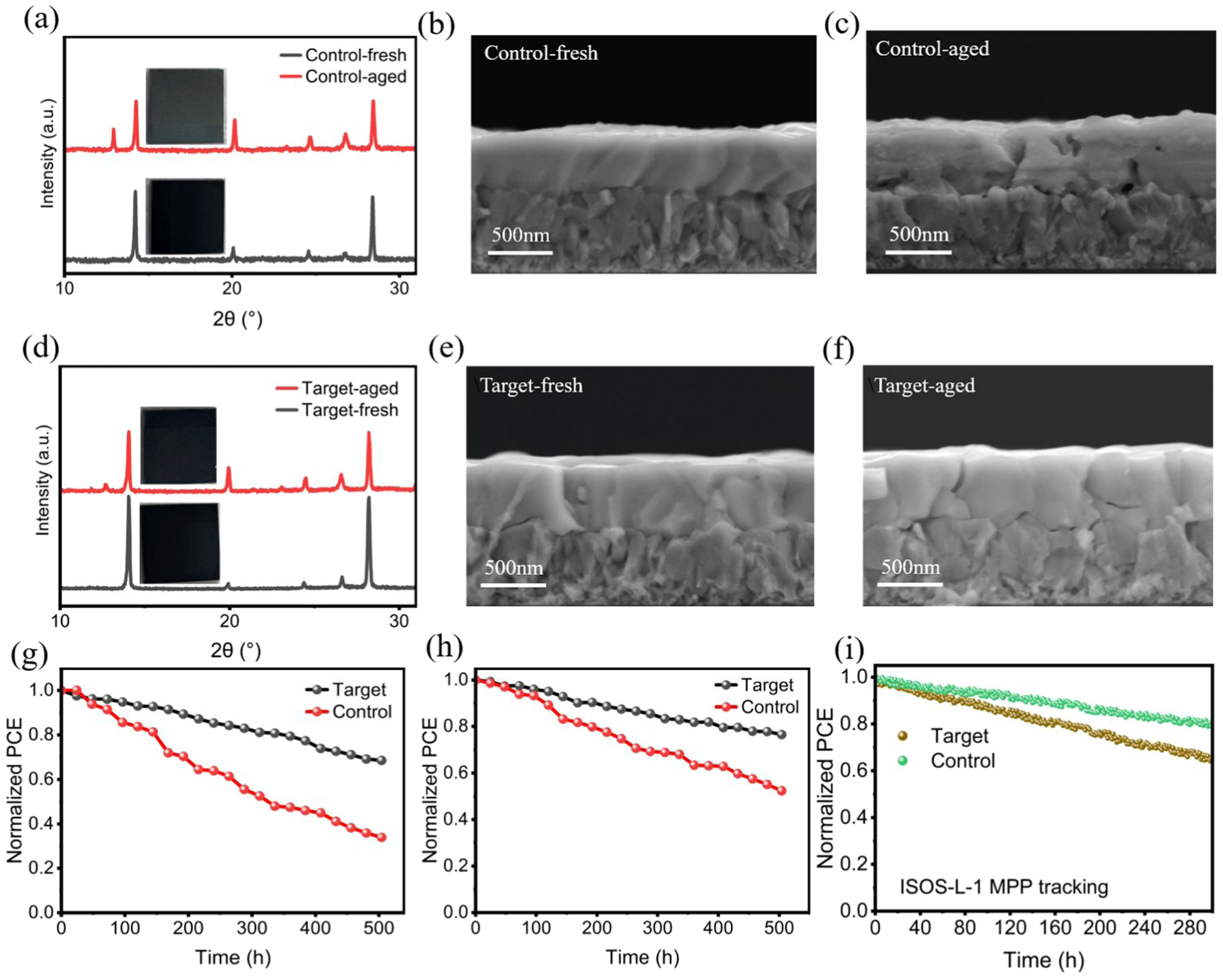

Figure 6. (a−c) XRD spectra and SEM images of the fresh and aged control films; (d−f) XRD spectra and SEM images of the fresh and aged target films; (g) efficiency attenuation of the control and target devices after being stored for 500 h under the conditions of 25 °C and 60% RH; (h) efficiency attenuation of the control and target devices after continuous heating at 85 °C for 500 h in nitrogen atmosphere; (i) ISOS-L-1 MPP tracking for 300 h.

pressed. The distribution of PL intensity demonstrates the uniformity of the film, which is conducive to the carrier transport at the interface.[29] The positive effect of 4-PBA on perovskite films was further confirmed by PL and time-resolved photoluminescence (TRPL) (Figure 3c,d). The average carrier lifetime (τ_{avg}) of the 4-PBA film deposited on the insulating substrate is 574.26 ns, which is longer than 396.62 ns of the pristine film, while the τ_{avg} of the 4-PBA film deposited on the SnO_2 substrate is 107.71 ns, which is lower than the 193.74 ns of the initial film. The passivation effect of 4-PBA suppresses the nonradiative recombination of perovskite, increases the carrier lifetime, and enhances the carrier separation efficiency. The microstructure of the perovskite was characterized through X-ray diffraction (XRD) testing. In the $\theta-2\theta$ scanning mode, the diffraction peak intensity of the 4-PBA film is larger than that of the pristine film (Figure S8, Supporting Information). Furthermore, ultraviolet−visible (UV−vis) light absorption testing revealed that the optical bandgap of the perovskite remained unchanged (1.538 eV), while the absorption curve exhibits obvious improvement, which is conducive to the absorption of more photons (Figure S9, Supporting Information). The XRD and UV−vis results indicate that the crystallinity of the perovskite films has been enhanced, implying a lower defect density, which is conducive to the fabrication of higher efficiency devices. Furthermore, the residual stress in the perovskite films was characterized through grazing incidence X-ray diffraction (GIXRD) (Figure 3e,f). Residual stress in perovskite films is considered an important factor influencing carrier dynamics and device stability, which increases interfacial charge recombination and hinders charge transfer, accelerating the degradation of perovskite and adversely affecting device stability.[30,31] A linear fit of the $d-\omega$ data revealed that the slope of the line decreased from 0.091 to 0.069, indicating a reduction in the residual stress within the films, which can improve the long-term stability of the perovskite films (Figure 3g).

2.3. Device Performance and Defect Density. Based on the perovskite/4-PBA codeposition strategy, the device with FTO/SnO_2/PVSK/Spiro-OMeTAD/MoO_3/Ag structure was fabricated. By optimizing the doping concentration of 4-PBA (0.5 mg mL^{-1}), the champion PCE is 24.91%, and the enhanced performance is attributed to improvements in V_{OC}

and fill factor (FF) (Figures 4a and S10). The hysteresis factor of the target device is significantly lower than that of the control device, which benefits from the accelerated interfacial extraction and the reduced interfacial recombination (Figure 4b). The integral current density of the target device is 24.96 mA cm^{-2}, and that of the control device is 24.76 mA cm^{-2}, which match well with the J_{SC} obtained from the $J-V$ testing (Figure 4c). Moreover, the output of the target device at the maximum power point remains relatively stable within 200 s (Figure 4d).

We investigated the dark $J-V$ characteristics of electron-only devices with a perovskite film thickness of 700 nm to quantify the defect density (Figure S11, Supporting Information). The V_{TFL} for the control sample is 0.342 V, while the V_{TFL} for the target sample is 0.258 V. The defect density of the control device is 1.135×10^{17} cm^{-3}, while that of the control device is 1.505×10^{17} cm^{-3} (Figure 5a). The dark current test and ideal factor test further demonstrate the defect passivation of 4-PBA in the PSCs. The dark current of the target device is 9×10^{-7} mA, which is much lower than the dark current 8×10^{-6} mA of the control device, while the ideality factor fitted from the V_{OC}-light intensity dependence data also decreases from 1.46 of the control device to 1.29 of the target device (Figure 5b,c). Both the lower dark current and the smaller ideality factor indicate that the defect density inside the device has decreased.

The electrochemical impedance spectroscopy (EIS) experiment (Figure 5d) was carried out on the control device and target device to investigate the carrier recombination behavior. Compared with the control device, the target device exhibited a smaller series resistance (R_s) and a larger recombination resistance (R_{rec}), indicating rapid charge transfer and reduced carrier recombination, which is consistent with the enhanced FF (Table S2, Supporting Information).[32] Furthermore, in order to expound on the increase in V_{OC}, the Mott−Schottky test was performed in a dark environment. The estimated built-in potential (V_{bi}) increased from 0.84 V in the control device to 0.93 V in the target device, indicating that the introduction of 4-PBA increases the driving force for carrier separation, resulting in the high V_{OC} of the target device (Figure 5e). As illustrated in Figure 5f, the modification effect of 4-PBA on the interface results in the reduction of the interface charge density (N_{IF}) from 3.26×10^{18} to 6.54×10^{17} cm^{-3}, indicating the decrease in defect density.[33]

2.4. Stability of the Films and PSCs. Finally, the stability performance of the perovskite films and PSCs was investigated. As shown in Figure 6a, compared with the fresh control film, the signal of PbI_2 generated by perovskite decomposition in the XRD pattern of the aged control film stored in ambient air at 25 °C and 20% RH for 2000 h is very obvious. The SEM images exhibit a significant morphological change following the degradation of the perovskite (Figure 6b,c). However, a weak lead iodide signal is generated in the XRD pattern of the target film, indicating that the degradation degree of the target thin film is very low. It can also be seen from the SEM image that there is no obvious change in the morphology of the fresh and aged thin films (Figure 6d−f).

Subsequently, the stability of PSCs under moisture, heat, and illumination conditions was investigated. The PSCs structure for the stability test is FTO/SnO_2/PVSK/PEAI/MoO_3/Ag. After the devices without encapsulation were stored at 25 °C and 60% RH for 500 h, the PCE of the target device is 68.6% of the initial efficiency, while that of the control device remains only 33.9%. After being heated at 85 °C for 500 h in a nitrogen atmosphere, the PCE of the target device is 76.5% of the original efficiency, while that of the control device is 52.4%. Finally, the PCE of the target device was 81% of the initial efficiency under the ISOS-L-1 MPP tracking for 300h, while that of the control device decreased to 66%.

3. CONCLUSIONS

We report a codeposition strategy that enhances the efficiency and stability of the n−i−p PSCs by adding 4-PBA molecules into the perovskite precursors. The phosphonic acid groups of 4−PBA molecules promote the adsorption of 4-PBA on the SnO_2 surface. The anchored molecules can effectively passivate the defects on the SnO_2 surface, and the bromine atoms can coordinate with uncoordinated Pb^{2+} on the buried interface. Thus, 4-PBA serves as a molecular bridge connecting the ETL and perovskite layer, facilitating the separation of carriers at the interface. It improves the perovskite morphology and enhances perovskite crystallization. The 4-PBA PSCs achieve a PCE of 24.9%, with a V_{OC} of 1.161 V and an FF of 84.26%, which is higher than that of the control device (23.79%). The PSCs based on 4-PBA exhibit excellent long-term stability. This study proposes a new method for interface passivation, aiming to improve the efficiency and stability of PSCs.

4. METHODS AND MATERIALS

4.1. Materials. Anhydrous solvents including *N*,*N*-dimethylformamide (DMF), dimethyl sulfoxide (DMSO), chlorobenzene (CB), isopropanol (IPA), 4-*tert*-butyl-pyridine (TBP), and acetonitrile (ACN) were purchased from Sigma-Aldrich. Lead iodide (PbI_2, 99.99%) and (4-bromophenyl) phosphonic acid (4-PBA) were purchased from TCI. Formamidinium iodide (FAI, 99.99%), methylammonium iodide (MAI), and methylammonium chloride (MACl, 99.9%) were purchased from Great Solar Cell. Cesium iodide (CsI, 99.999%) was purchased from Advanced Election Technology Co., Ltd. (China). Lithium bis (trifluoromethanesulfonyl) imide salt (Li-TFSI) was purchased from Sigma-Aldrich. FK209-Co(III)-TFSI was purchased from Great Solar Cell. Bathocuproine (BCP, >99%), phenyl-C61-butyric acid methyl ester (PC61BM, >99%), and Spiro-OMeTAD were purchased from Xi'an Polymer Light Technology Corp. (China).

4.2. Preparation of Perovskite Precursor Solution. 1.6 M $Cs_{0.05}FA_{0.9}MA_{0.05}PbI_3$ was dissolved in 800 μL of DMF and 800 μL of DMSO solution (volume ratio 4:1) with 20 mol % MACl and 5 mol % PbI_2, and stirred overnight to prepare undoped precursor solution. For doped solution, another 0.1−1.0 mg of 4-PBA was added in the preceding solution.

4.3. Device Fabrication. The FTO substrate was subjected to ultrasonic cleaning sequentially with deionized water, acetone, 2-propanol, and ethanol, followed by nitrogen drying. Subsequently, SnO_2 electron transport layer was deposited based on previous work.[34] During the last 10 s of the spin-coating process, 120 μL of chlorobenzene was dynamically spun as an antisolvent to facilitate the crystallization of perovskite, followed by annealing at 120 °C for 40 min in air with a relative humidity of 25% RH. Then, the Spiro-OMeTAD solution (4500 rpm for 30 s) is composed of 1 mL of chlorobenzene solution of Spiro-OMeTAD powder (73 mg mL^{-1}), 18 μL of acetonitrile solution of lithium salt (520 mg mL^{-1}), and 29 μL of TBP. At last, the metal electrode with a thickness of 100 nm was evaporated through a metal mask.

4.4. Characterizations. TOF-SIMS was carried out on TOF-SIMS 5 (ION-TOF GmbH, Germany). The DLS test was conducted by a nanoparticle size and ζ potential analyzer (Omni, USA). The FTIR spectra were characterized by an iN10 MX (Thermo, USA). XPS and UPS were conducted using the AXIS-UltraDLD (Kratos) with a fine scanning step of 0.01 eV. The XRD patterns were measured by DX-2700BH. The UV−vis spectra were measured by UV-2600, Shimadzu. The PL and TRPL spectra were conducted with

FLS1000 (Edinburgh Instruments, U.K.). The PL mapping test was carried out on the RISE-MAGNA (TESCAN, Czech). The EQE measurement was conducted on a QEX10. The *J*−*V* test was carried out with a Keithley 2400 source meter, and the illumination (AM 1.5G, 100 mW cm^{-2}, 25 °C) was provided by an Enlitech SS-X simulator. The unencapsulated devices were measured both in reverse scan (1.2 V → −0.2 V, step 0.01 V) and forward scan (−0.2 V → 1.2 V, step 0.01 V) with a 200 ms delay time. The active area is defined by the shade mask to be 0.0525 cm^2. The *C*−*V* (10 kHz with a voltage amplitude of 10 mV) and EIS tests were conducted using the electrochemical workstation V89143, VERTEX.

■ ASSOCIATED CONTENT

Data Availability Statement

The data that support the findings of this study are available from the corresponding author upon reasonable request.

Supporting Information

The Supporting Information is available free of charge at https://pubs.acs.org/doi/10.1021/acsami.5c02282.

> Characterization and measurements, molecular structure of 4-PBA, three-dimensional spatial distribution mapping, DLS spectra, FTIR spectra, XPS spectra, UPS spectra, XRD spectra, UV−vis curve, SEM images, statistics graphs of photovoltaic parameter, and fitting results of TRPL and EIS curves (PDF)

■ AUTHOR INFORMATION

Corresponding Author

Wenzhong Shen − *Institute of Solar Energy, and Key Laboratory of Artificial Structures and Quantum Control (Ministry of Education), School of Physics and Astronomy, Shanghai Jiao Tong University, Shanghai 200240, People's Republic of China; Shanghai Non-carbon Energy Conversion and Utilization Institute, Shanghai 200240, People's Republic of China;* orcid.org/0000-0003-4527-9183; Email: wzshen@sjtu.edu.cn

Authors

Dezhao Zhang − *Institute of Solar Energy, and Key Laboratory of Artificial Structures and Quantum Control (Ministry of Education), School of Physics and Astronomy, Shanghai Jiao Tong University, Shanghai 200240, People's Republic of China; Shanghai Non-carbon Energy Conversion and Utilization Institute, Shanghai 200240, People's Republic of China;* orcid.org/0009-0005-4337-2626

Li He − *Institute of Solar Energy, and Key Laboratory of Artificial Structures and Quantum Control (Ministry of Education), School of Physics and Astronomy, Shanghai Jiao Tong University, Shanghai 200240, People's Republic of China; Shanghai Non-carbon Energy Conversion and Utilization Institute, Shanghai 200240, People's Republic of China*

Haotian Zhang − *Institute of Solar Energy, and Key Laboratory of Artificial Structures and Quantum Control (Ministry of Education), School of Physics and Astronomy, Shanghai Jiao Tong University, Shanghai 200240, People's Republic of China; Shanghai Non-carbon Energy Conversion and Utilization Institute, Shanghai 200240, People's Republic of China*

Hongzhen Su − *Institute of Solar Energy, and Key Laboratory of Artificial Structures and Quantum Control (Ministry of Education), School of Physics and Astronomy, Shanghai Jiao Tong University, Shanghai 200240, People's Republic of China; Shanghai Non-carbon Energy Conversion and Utilization Institute, Shanghai 200240, People's Republic of China;* orcid.org/0000-0002-3584-8138

Yusong Zhou − *Institute of Solar Energy, and Key Laboratory of Artificial Structures and Quantum Control (Ministry of Education), School of Physics and Astronomy, Shanghai Jiao Tong University, Shanghai 200240, People's Republic of China; Shanghai Non-carbon Energy Conversion and Utilization Institute, Shanghai 200240, People's Republic of China;* orcid.org/0009-0006-2745-328X

Wan Li − *Institute of Solar Energy, and Key Laboratory of Artificial Structures and Quantum Control (Ministry of Education), School of Physics and Astronomy, Shanghai Jiao Tong University, Shanghai 200240, People's Republic of China; Shanghai Non-carbon Energy Conversion and Utilization Institute, Shanghai 200240, People's Republic of China*

Shuxin Cui − *Institute of Solar Energy, and Key Laboratory of Artificial Structures and Quantum Control (Ministry of Education), School of Physics and Astronomy, Shanghai Jiao Tong University, Shanghai 200240, People's Republic of China; Shanghai Non-carbon Energy Conversion and Utilization Institute, Shanghai 200240, People's Republic of China*

Hong Liu − *Institute of Solar Energy, and Key Laboratory of Artificial Structures and Quantum Control (Ministry of Education), School of Physics and Astronomy, Shanghai Jiao Tong University, Shanghai 200240, People's Republic of China; Shanghai Non-carbon Energy Conversion and Utilization Institute, Shanghai 200240, People's Republic of China;* orcid.org/0000-0002-2241-1199

Complete contact information is available at: https://pubs.acs.org/10.1021/acsami.5c02282

Author Contributions

CRediT: D.Z.: writing—original draft, methodology, investigation, data curation. L.H.: writing—original draft, investigation, data curation. H.Z.: writing—review and editing, supervision, resources. H.S.: methodology, investigation. Y.Z.: methodology, investigation. W.L.: validation, investigation. S.C.: validation, supervision. H.L.: writing—review and editing, supervision, resources. W.S.: writing—review and editing, supervision, funding acquisition.

Notes

The authors declare no competing financial interest.

■ ACKNOWLEDGMENTS

This work was supported by the Shanghai New Energy Technology Research and Development Project of China (Grant No. 24DZ3000900) and the National Natural Science Foundation of China (Grant No. 11834011).

■ REFERENCES

(1) Li, H.; Xie, G.; Fang, J.; Wang, X.; Li, S.; Lin, D.; Wang, D.; Huang, N.; Peng, H.; Qiu, L. Holistic dielectric and buffer interfacial layers enable high-efficiency perovskite solar cells and modules. *Nano Energy* **2024**, *124*, No. 109507.

(2) Wang, H.; Zheng, Y.; Zhang, G.; Wang, P.; Sui, X.; Yuan, H.; Shi, Y.; Zhang, G.; Ding, G.; Li, Y.; et al. In Situ Dual-Interface Passivation Strategy Enables The Efficiency of Formamidinium Perovskite Solar Cells Over 25%. *Adv. Mater.* **2024**, *36* (6), No. 2307855.

(3) Ge, Y.; Zheng, L.; Wang, H.; Gao, J.; Yao, F.; Wang, C.; Li, G.; Guan, H.; Wang, S.; Cui, H.; et al. Suppressing wide-angle light loss

and non-radiative recombination for efficient perovskite solar cells. *Nat. Photonics* **2025**, *19*, 170.

(4) Han, C.; Wu, Y.; Xu, G.; Wu, X.; Xu, J.; Xu, T.; Huang, S.; Shen, Y.; Cao, Z.; Chen, W.; et al. Program-Modulated Kinetics of Perovskite-Film Growth by Molecular "Thruster" for High-Efficiency and Stable Perovskite Solar Cells. *Angew. Chem., Int. Ed.* **2025**, *64*, No. e202419726.

(5) Shin, Y. S.; Song, J. W.; Lee, D. G.; Lee, J.; Seo, J.; Roe, J.; Shin, G. Y.; Kim, D.; Yeop, J.; Lee, D.; et al. De-doping engineering for efficient and heat-stable perovskite solar cells. *Joule* **2025**, *9* (1), No. 101779.

(6) Li, F.; Deng, X.; Shi, Z.; Wu, S.; Zeng, Z.; Wang, D.; Li, Y.; Qi, F.; Zhang, Z.; Yang, Z.; et al. Hydrogen-bond-bridged intermediate for perovskite solar cells with enhanced efficiency and stability. *Nat. Photonics* **2023**, *17* (6), 478−484.

(7) Liang, Z.; Zhang, Y.; Xu, H.; Chen, W.; Liu, B.; Zhang, J.; Zhang, H.; Wang, Z.; Kang, D.-H.; Zeng, J.; et al. Homogenizing out-of-plane cation composition in perovskite solar cells. *Nature* **2023**, *624* (7992), 557−563.

(8) Liu, C.; Yang, Y.; Chen, H.; Xu, J.; Liu, A.; Bati, A. S. R.; Zhu, H.; Grater, L.; Hadke, S. S.; Huang, C.; et al. Bimolecularly passivated interface enables efficient and stable inverted perovskite solar cells. *Science* **2023**, *382* (6672), 810−815.

(9) He, L.; Su, H.; Li, Z.; Liu, H.; Shen, W. Multiple Function Synchronous Optimization by PbS Quantum Dots for Highly Stable Planar Perovskite Solar Cells with Efficiency Exceeding 23%. *Adv. Funct. Mater.* **2023**, *33* (17), No. 2213963.

(10) Zou, H.; Bi, H.; Chen, Y.; Guo, M.; Hou, W.; Su, P.; Zhou, K.; Yang, C.; Gong, X.; Xiao, L.; Liu, L. Functionalized polymer modified buried interface for enhanced efficiency and stability of perovskite solar cells. *Nanoscale* **2023**, *15* (5), 2054−2060.

(11) Khadka, D. B.; Shirai, Y.; Yanagida, M.; Ota, H.; Lyalin, A.; Taketsugu, T.; Miyano, K. Defect passivation in methylammonium/bromine free inverted perovskite solar cells using charge-modulated molecular bonding. *Nat. Commun.* **2024**, *15* (1), No. 882.

(12) Sun, W.; Wang, K.; Liu, W.; Huo, X.; Yin, R.; Sun, Y.; Gao, Y.; You, T.; Yin, P. Bidirectional Modification of Buried Interface Reduces Energy Loss for Planar Perovskite Solar Cells with Efficiency > 23%. *Sol. RRL* **2023**, *7* (5), No. 2200991.

(13) Zheng, X.; Li, Z.; Zhang, Y.; Chen, M.; Liu, T.; Xiao, C.; Gao, D.; Patel, J. B.; Kuciauskas, D.; Magomedov, A.; et al. Co-deposition of hole-selective contact and absorber for improving the processability of perovskite solar cells. *Nat Energy* **2023**, *8* (5), 462−472.

(14) Wang, W.; Li, X.; Huang, P.; Yang, L.; Gao, L.; Jiang, Y.; Hu, J.; Gao, Y.; Che, Y.; Deng, J.; Zhang, J.; Tang, W. In situ Blending For Co-Deposition of Electron Transport and Perovskite Layers Enables Over 24% Efficiency Stable Conventional Solar Cells. *Adv. Mater.* **2024**, *36* (36), No. 2407349.

(15) Zhang, B.; Oh, J.; Sun, Z.; Cho, Y.; Jeong, S.; Chen, X.; Sun, K.; Li, F.; Yang, C.; Chen, S. Buried Guanidinium Passivator with Favorable Binding Energy for Perovskite Solar Cells. *ACS Energy Lett.* **2023**, *8* (4), 1848−1856.

(16) Wang, L.; Xia, J.; Yan, Z.; Song, P.; Zhen, C.; Jiang, X.; Shao, G.; Qiu, Z.; Wei, Z.; Qiu, J.; Nazeeruddin, M. K. Robust Interfacial Modifier for Efficient Perovskite Solar Cells: Reconstruction of Energy Alignment at Buried Interface by Self-Diffusion of Dopants. *Adv. Funct. Mater.* **2022**, *32* (35), No. 2204725.

(17) Xu, R.; Pan, F.; Chen, J.; Li, J.; Yang, Y.; Sun, Y.; Zhu, X.; Li, P.; Cao, X.; Xi, J.; et al. Optimizing the Buried Interface in Flexible Perovskite Solar Cells to Achieve Over 24% Efficiency and Long-Term Stability. *Adv. Mater.* **2024**, *36* (7), No. 2308039.

(18) Guo, H.; Xiang, W.; Fang, Y.; Li, J.; Lin, Y. Molecular Bridge on Buried Interface for Efficient and Stable Perovskite Solar Cells. *Angew. Chem., Int. Ed.* **2023**, *62* (34), No. e202304568.

(19) Cheng, C.; Yao, Y.; Li, L.; Zhao, Q.; Zhang, C.; Zhong, X.; Zhang, Q.; Gao, Y.; Wang, K. A Novel Organic Phosphonate Additive Induced Stable and Efficient Perovskite Solar Cells with Efficiency over 24% Enabled by Synergetic Crystallization Promotion and Defect Passivation. *Nano Lett.* **2023**, *23* (19), 8850−8859.

(20) Chen, H.; Liu, C.; Xu, J.; Maxwell, A.; Zhou, W.; Yang, Y.; Zhou, Q.; Bati, A. S. R.; Wan, H.; Wang, Z.; et al. Improved charge extraction in inverted perovskite solar cells with dual-site-binding ligands. *Science* **2024**, *384* (6692), 189−193.

(21) Li, C.; Chen, Y.; Li, Y.; Gong, L.; Yuan, Z.; Liang, L.; Chen, J.; Ganesan, P.; Zhang, Y.; Ma, J.; et al. Deciphering the Impact of Aromatic Linkers in Self-Assembled Monolayers on the Performance of Monolithic Perovskite/Si Tandem Photovoltaic. *Angew. Chem., Int. Ed.* **2025**, *64*, No. e202420585.

(22) Li, T.; Wang, K.; Tong, Y.; Qi, H.; Yue, S.; Li, W.; Wang, H. In Situ Dehydration Condensation of Self-Assembled Molecules Enables Stabilization of CsPbI3 Perovskites for Efficient Photovoltaics. *Adv. Funct. Mater.* **2024**, *34* (51), No. 2409621.

(23) Li, M.; Jiao, B.; Peng, Y.; Zhou, J.; Tan, L.; Ren, N.; Ye, Y.; Liu, Y.; Yang, Y.; Chen, Y.; et al. High-Efficiency Perovskite Solar Cells with Improved Interfacial Charge Extraction by Bridging Molecules. *Adv. Mater.* **2024**, *36* (38), No. 2406532.

(24) Tan, Q.; Li, Z.; Luo, G.; Zhang, X.; Che, B.; Chen, G.; Gao, H.; He, D.; Ma, G.; Wang, J.; et al. Inverted perovskite solar cells using dimethylacridine-based dopants. *Nature* **2023**, *620* (7974), 545−551.

(25) Duan, C.; Gao, H.; Xiao, K.; Yeddu, V.; Wang, B.; Lin, R.; Sun, H.; Wu, P.; Ahmed, Y.; Bui, A. D.; et al. Scalable fabrication of wide-bandgap perovskites using green solvents for tandem solar cells. *Nat. Energy* **2025**, *10*, 318−328.

(26) Li, S.; Zheng, Z.; Ju, J.; Cheng, S.; Chen, F.; Xue, Z.; Ma, L.; Wang, Z. A Generic Strategy to Stabilize Wide Bandgap Perovskites for Efficient Tandem Solar Cells. *Adv. Mater.* **2024**, *36* (9), No. 2307701.

(27) Zhang, C.; Shen, X.; Chen, M.; Zhao, Y.; Lin, X.; Qin, Z.; Wang, Y.; Han, L. Constructing a Stable and Efficient Buried Heterojunction via Halogen Bonding for Inverted Perovskite Solar Cells. *Adv. Energy Mater.* **2023**, *13* (2), No. 2203250.

(28) Wei, Y.; Tang, Y.; Li, H.; Zhang, G.; Chen, H.; Liu, S.; Zhang, Z.; Li, H.; An, B.; Liu, X.; Wang, H. Decreased Hysteresis Benefited from Enhanced Lattice Oxygen and Promoted Band Alignment with Electron Transport Layer Modification in Perovskite Solar Cells. *ACS Appl. Mater. Interfaces* **2025**, *17* (7), 11278−11286.

(29) Luo, C.; Zheng, G.; Gao, F.; Wang, X.; Zhan, C.; Gao, X.; Zhao, Q. Engineering the buried interface in perovskite solar cells via lattice-matched electron transport layer. *Nat. Photonics* **2023**, *17* (10), 856−864.

(30) Meng, W.; Zhang, K.; Osvet, A.; Zhang, J.; Gruber, W.; Forberich, K.; Meyer, B.; Heiss, W.; Unruh, T.; Li, N.; Brabec, C. J. Revealing the strain-associated physical mechanisms impacting the performance and stability of perovskite solar cells. *Joule* **2022**, *6* (2), 458−475.

(31) Tao, M.; Wang, Y.; Zhang, K.; Song, Z.; Lan, Y.; Guo, H.; Guo, L.; Zhang, X.; Wei, J.; Cao, D.; Song, Y. Molecule-triggered strain regulation and interfacial passivation for efficient inverted perovskite solar cells. *Joule* **2024**, *8* (11), 3142−3152.

(32) Liu, P.; Xiang, H.; Wang, W.; Ran, R.; Zhou, W.; Shao, Z. A bilateral cyano molecule serving as an effective additive enables high-efficiency and stable perovskite solar cells. *J. Energy Chem.* **2021**, *62*, 243−251.

(33) Qiao, F.; Du, D.; Shen, W.; Wang, W.; Chen, Z.; Gao, C.; He, L.; Lü, Z.; Liu, H. Synergetic Acceleration on the Degradation of Flexible Perovskite Solar Cells under Light and Stress Cooperation. *Sol. RRL* **2023**, *7* (15), No. 2300331.

(34) Zhang, D.; Du, D.; Zhang, H.; Su, H.; Gao, C.; Li, Z.; Liu, H.; Shen, W. Interface and bulk engineering by dual sulfonates toward high efficiency perovskite solar cells with better reproducibility and stability. *Sol. Energy Mater. Sol. Cells* **2024**, *277*, No. 113071.